Photoinduced structural dynamics of multiferroic TbMnO₃

Elsa Abreu [●],[1,*] Matteo Savoini [●],[1] Larissa Boie [●],[1] Paul Beaud [●],[2] Vincent Esposito,[2] Martin Kubli,[1]
Martin J. Neugebauer [●],[1] Michael Porer,[2] Urs Staub [●],[2] Seyed M. Koohpayeh,[3] Bulat Burganov,[1] Chris Dornes,[1]
Angel Rodriguez-Fernandez [●],[2] Lucas Huber,[1] Gabriel Lantz,[1] José R. L. Mardegan,[2] Sergii Parchenko,[2] Jochen Rittmann,[2]
Cris Svetina,[2] Gerhard Ingold,[2] and Steven L. Johnson [●][1,2,†]

[1]*Institute for Quantum Electronics, Eidgenössische Technische Hochschule (ETH) Zürich, 8093 Zürich, Switzerland*
[2]*Paul Scherrer Institut, 5232 Villigen, Switzerland*
[3]*Institute for Quantum Matter (IQM), Department of Physics and Astronomy, Johns Hopkins University, Baltimore, Maryland 21218, USA*

We use time-resolved hard x-ray diffraction to investigate the structural dynamics of the multiferroic insulator
TbMnO₃ in the low-temperature antiferromagnetic and ferroelectrically ordered phase. The lattice response
following photoexcitation at 1.55 eV is detected by measuring the (0 2 4) and (1 3 −5) Bragg reflections. A
0.022% tensile strain, normal to the surface, is seen to arise within 20–40 ps. The magnitude of this transient
strain is over an order of magnitude lower than that predicted from laser-induced heating, which we attribute
to a bottleneck in the energy transfer between the electronic and lattice subsystems. The timescale for the
transient expansion is consistent with that of previously reported demagnetization dynamics. We discuss a
possible relationship between structural and demagnetization dynamics in TbMnO₃, in which photoinduced
atomic motion modulates the exchange interaction, leading to a destruction of the magnetic order in the system.

I. INTRODUCTION

Rare-earth manganites are prime examples of complex
materials, where a rich phase diagram is driven by a subtle
interplay of charge, spin, orbital, and structural degrees of
freedom. Identifying the role of each degree of freedom in the
determination of key physical properties in such materials is
essential but often extremely challenging. One way to address
this challenge is to use pump-probe measurements to explore
how different degrees of freedom respond to being driven out
of equilibrium.

Here we focus on insulating TbMnO₃, a prototypical
multiferroic with an orthorhombically distorted perovskite
structure (space group *Pbnm*), which exhibits two magnetic
phase transitions, at $T_{N_1} = 42$ K and $T_{N_2} = 27$ K, driven by
ordering of the Mn $3d$ spins [1]. Below T_{N_1}, TbMnO₃ is
ferromagnetic along the *a* axis, antiferromagnetic along *c*,
and it exhibits an antiferromagnetic sinusoidal spin density
wave order along *b*. Below T_{N_2}, a magnetic cycloid forms in
the *bc* plane which gives rise to a ferroelectric polarization
along the *c* axis. Pump-probe experiments in the multiferroic
phase $(T < T_{N_2})$ [2–7] have shown that the antiferromagnetic
order decreases on a 20–40 ps timescale in response to strong
photoexcitation at photon energies of 1.55 and 3 eV, which
directly excite an intersite Mn $3d$ transition and an O $2p \rightarrow$
Mn $3d$ transition, respectively [8,9]. A phenomenological
model [4] has associated this decrease in magnetic order to an
increase in effective spin temperature, from 12 K up to about
45 K for an absorbed fluence of 9.0 mJ/cm². It is, however,
still unclear exactly how the electronic transitions excited by
the pump pulse couple to the magnetism, although several
different hypotheses have been suggested [4,6,7,10]. In this
work, we investigate the structural dynamics of TbMnO₃ us-
ing ultrafast hard x-ray diffraction in an attempt to investigate
a potential contribution of the lattice to this process.

II. METHODS

The experiments were performed at the FEMTO slicing
beamline of the Swiss Light Source at the Paul Scherrer Insti-
tute [11], using a gated two-dimensional Pilatus detector [12].
Bulk [010]-cut samples of TbMnO₃ were cooled down to ap-
proximately 20 K using a liquid helium jet. The temperature at
the sample position was calibrated in advance and monitored
throughout the experiment with the help of a temperature
sensor placed next to the sample. To prevent freezing of water
or nitrogen on the sample, a box was built around it and
purged with helium gas. The *p*-polarized 1.55-eV pump beam
and the monochromatic 7.05-keV x-ray probe beam were
incident from the same direction but with different grazing
incidence angles on the sample: 5.5° (or 10.2°, in a subsequent
experiment) for the pump and 0.5° for the probe. The inten-
sity profile of the pump beam had a penetration depth $(1/e)$,
normal to the surface, of 323 nm for a polarization along the
crystallographic *a* axis and 671 nm for a polarization along
the crystallographic *c* axis [7]. The electric field profile of
the x-ray probe had a penetration depth $(1/e)$ of 76 nm [13].
The pumped area was about four times larger than the probed
area. The pump beam diameter was monitored throughout the
experiment on a beam profiling camera placed at the same
downstream position as the sample but on a parallel path,
starting at a leakage from a mirror. The pump and probe pulses
have full width at half-maximum durations of about 100 and
120 fs and repetition rates of 1 and 2 kHz, respectively. The

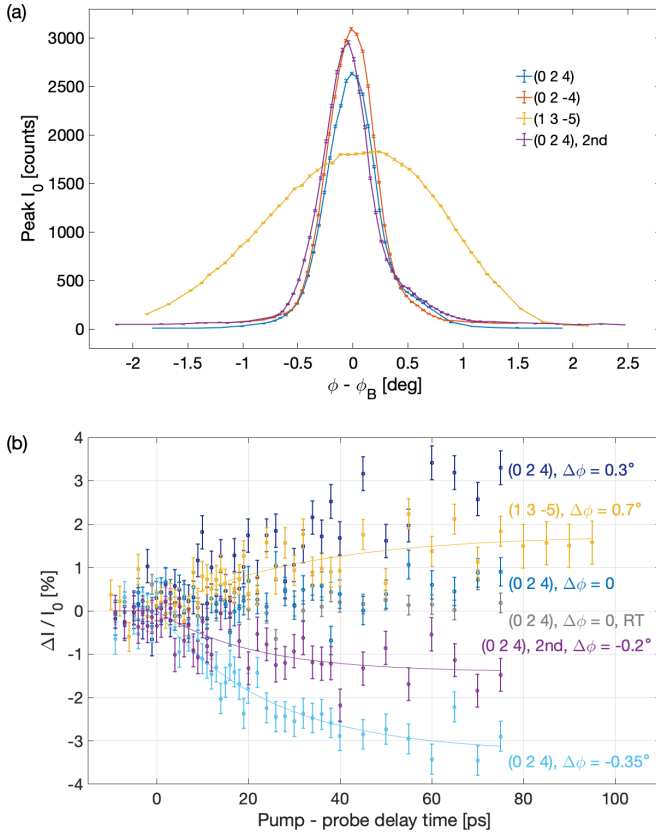*elsabreu@phys.ethz.ch
†johnson@phys.ethz.ch

FIG. 1. (a) Equilibrium ϕ scan of the relevant Bragg reflections, at $T = 20$ K. (b) Pump-probe delay traces at fixed $\Delta\phi = \phi - \phi_B$ positions and for different Bragg reflections, as labeled. All data were taken at $T = 20$ K except for the trace labeled RT (room temperature). The $(1\ 3\ -5)$ trace was acquired at a pump fluence of 4.5 mJ/cm^2, the others at 9.0 mJ/cm^2. Full lines are fits to Eq. (1).

temporal overlap between the two pulses was determined by time-resolved x-ray diffraction measurements performed on bulk [411]-cut bismuth samples at the start of the experiment, for calibration [14].

III. EXPERIMENTAL RESULTS

Figure 1(a) shows the variation in intensity I_0 of four lattice reflections as a function of $\phi - \phi_B$, where ϕ is the angle of rotation of the sample around the normal to its surface and ϕ_B is the value of ϕ that maximizes a particular diffraction peak. Here, the intensity I_0 is taken as the number of photons detected during one second in a region of the detector containing the diffraction peak, for a particular value of ϕ. Data are shown for the $(0\ 2\ 4)$ and $(1\ 3\ -5)$ Bragg reflections, as well as for $(0\ 2\ -4)$. Note that for the low-temperature phase of TbMnO$_3$ (space group *Pbnm*), $(0\ 2\ -4)$ is equivalent to $(0\ 2\ 4)$ and exhibits the same dynamics in this [010]-cut sample geometry, so that data from the two reflections are equivalent. A second ϕ scan for $(0\ 2\ 4)$, measured during a subsequent experiment, is also included in Fig. 1(a) as a reproducibility check. A small background intensity is visible in some ϕ scans, due to incoherent light scattering onto the detector. This contribution is, however, essentially independent of ϕ and therefore has no impact on the results and analysis presented below.

TABLE I. Summary of estimates for the parameter τ resulting from fitting the data of Fig. 1(b) (top three values) and Fig. 2 (bottom four values) to Eq. (1).

Reflection	Fluence (mJ/cm^2)	$\phi - \phi_B$	τ (ps)
$(0\ 2\ 4)$	9	$-0.35°$	24 ± 3
$(0\ 2\ 4)$, 2nd	9	$-0.2°$	21 ± 8
$(1\ 3\ -5)$	4.5	$0.7°$	31 ± 10
$(0\ 2\ 4)$	9	N/A	30 ± 10
$(0\ 2\ 4)$, 2nd	9	N/A	18 ± 5
$(0\ 2\ -4)$	4.5	N/A	19 ± 21
$(1\ 3\ -5)$	4.5	N/A	40 ± 16

We investigate the structural dynamics of TbMnO$_3$ by measuring the intensity diffracted from the $(0\ 2\ 4)$ and $(1\ 3\ -5)$ planes following photoexcitation. Given the scattering geometry dictated by these reflections at grazing incidence, the projection of the *p*-polarized 1.55-eV pump wave vector onto the sample surface forms 49° and 29° angles with respect to the crystallographic *c* axis for the $(0\ 2\ 4)$ and $(1\ 3\ -5)$ Bragg reflections, respectively.

Two types of time-resolved measurements were performed. In the first type, the value of ϕ is kept fixed and only the pump-probe delay is varied. Time traces obtained in this way for absorbed fluences of 4.5 and 9.0 mJ/cm^2 are presented in Fig. 1(b) for different ϕ values, Bragg reflections, and temperatures ($T = 20$ K and room temperature). The data are shown as the change in peak intensity following photoexcitation, $\Delta I(t) = I(t) - I_0$, relative to the unpumped case, I_0. No significant photoinduced effect is detected at the peak of the ϕ scan, for $\Delta\phi = \phi - \phi_B = 0$. Traces taken on the right (left) side of the ϕ scan, for $\phi - \phi_B > 0$ ($\phi - \phi_B < 0$), do show an increase (decrease) in $\Delta I(t)/I_0$, consistent with a shift of the peaks towards larger ϕ values. Fits were performed to a function of the form

$$f(t) = A\, H(t)\, [1 - \exp(-t/\tau)], \tag{1}$$

where $H(t)$ is the Heaviside function, and A and τ are fit parameters. The resulting fits are included in Fig. 1(b) for the three traces for which τ can be determined within a meaningful uncertainty such that $\tau > 2\,\delta\tau$, where $\delta\tau$ is the standard error. The fitted τ values are shown in Table I.

In the second type of measurements, full ϕ scans are measured at different pump-probe delays for the Bragg reflections shown in Fig. 1, and for absorbed fluences of 4.5 and 9.0 mJ/cm^2. This approach provides a more complete picture of the structural evolution of the system since it enables a distinction between changes in the ϕ integral of the Bragg peak intensity and shifts of the Bragg reflection along ϕ. The ϕ integral of the peak intensity is seen to remain unaffected by photoexcitation up to a pump-probe delay of 100 ps within the resolution of our measurement, which can detect changes larger than about 1%. A shift in the peak position along ϕ is, however, observed, as shown in Fig. 2. Each data point shown in Fig. 2 is calculated from the first moment of the ϕ scans

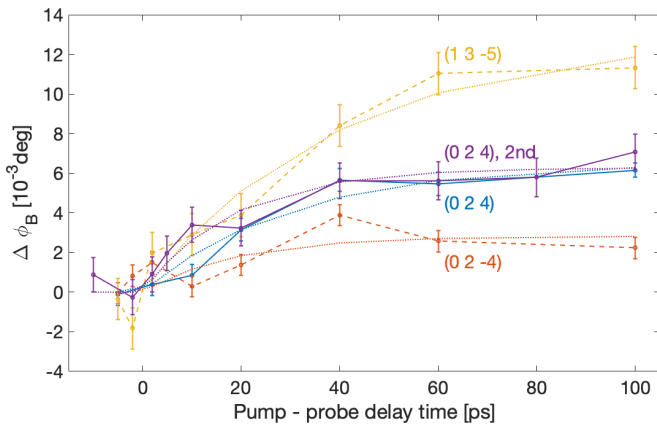$$\Delta\phi_B = \frac{\int (\phi - \phi_0) I(\phi)\, d\phi}{\int I(\phi)\, d\phi}, \tag{2}$$

FIG. 2. Photoinduced ϕ shift for different Bragg reflections, at $T = 20$ K. Full (dashed) lines correspond to an absorbed fluence of 9.0 mJ/cm^2 (4.5 mJ/cm^2). The error bars are estimated by bootstrapping. Dotted lines are fits to Eq. (1).

where ϕ_0 is chosen such that $\Delta\phi_B = 0$ for the unpumped sample, and the integration is carried out over the range of the scan in ϕ [Fig. 1(a)]. As seen in Fig. 1(a), the (1 3 −5) ϕ scan does not perfectly return to the baseline on the $\phi - \phi_B < 0$ side. This could lead to an overestimate of $\Delta\phi_B$ for the (1 3 −5) Bragg reflection presented in Fig. 2 but by no more than 10^{-3} deg, which is within the noise level of the measurements.[1] From Fig. 2 we see that $\Delta\phi_B$ is positive, as anticipated from the time traces in Fig. 1(b). The value of $\Delta\phi_B$ varies approximately linearly with fluence [comparing the (0 2 4) and (0 2 −4) data sets], and differs between Bragg reflections, as expected. Figure 2 also shows fits of each data set to Eq. (1). The fit parameters, all reported in Table I, yield timescales similar to those extracted from Fig. 1(b), although with overall larger uncertainties. It is clear from the data of Fig. 2 and from the fit results that the peak shift dynamics approach saturation within our 100-ps measurement window.

A conversion from $\Delta I(t)/I_0$ [Fig. 1(b)] to $\Delta\phi_B$ can also in principle be done, but it relies on an accurate determination of the derivative of the ϕ scan at the ϕ position chosen for the $\Delta I(t)/I_0$ measurement, as well as on the assumption that there is no change in the shape of the ϕ scan. We therefore opt to extract $\Delta\phi_B$ for Fig. 2 from the full ϕ-scan analysis, and use the data in Fig. 1(b) to obtain the timescales shown in Table I.

IV. ANALYSIS

The results presented in Sec. III show experimental evidence of a time-dependent change in the conditions for diffraction from certain lattice planes. Here we present a framework for understanding these changes in terms of the thermal and structural response of TbMnO3 to the pump excitation.

---

[1]The estimate was done by calculating $\Delta\phi_B$ with even more points removed on the $\phi - \phi_B < 0$ side. Removing up to four points reduced $\Delta\phi_B$ (100 ps) by less than 10^{-3} deg compared to the unaltered ϕ scan shown in Fig. 1(a), which is within the noise level of the measurements. Removing up to four points on the $\phi - \phi_B > 0$ side had no effect on the calculated $\Delta\phi_B$ value.

In TbMnO3, photons with an energy of 1.55 eV excite intersite d-d transitions between neighboring Mn^{3+} ions, creating Mn^{2+}-Mn^{4+} pairs [8,9]. This initially purely electronic energy is then partially transferred to the lattice as heat. One consequence of this lattice heating is an increase in dynamic, atomic-scale structural disorder over the region of the sample that has absorbed the pump light. This increase in disorder results in a change in the thermal stress over the heated region. On sufficiently long timescales, this change in thermal stress drives a change in lattice strain that can modify the lattice parameters of the crystal, and therefore modify the diffraction conditions.

In our experiment we are in principle sensitive to the increase in dynamic disorder via the Debye-Waller factor, which generally leads to a decrease in the peak efficiency of diffraction from a given lattice plane. We do not, however, observe a significant decrease of this efficiency for either the (0 2 4) or (1 3 −5) planes. This suggests that the increase in dynamic disorder, if present, is too small for our experiment to quantify directly.

Since the development of lattice strain modifies diffraction conditions, this is a likely cause of the observed time-dependent shifts in the optimal value of ϕ_B for diffraction. We now consider the quantitative connection between the thermal stress and the structural changes. The thermal stress due to heating can be generally written as

$$\sigma_{ij} = \sum_{kl} C_{ijkl}\big(\eta_{kl} - \eta_{kl}^{\Delta T}\big), \qquad (3)$$

where σ_{ij} are the components of the stress sensor in a Cartesian basis, C_{ijkl} are the components of the fourth-rank elastic stiffness tensor, $\eta_{kl} = (\partial u_k/\partial x_l + \partial u_l/\partial x_k)/2$ are the components of the strain tensor, and $\eta_{kl}^{\Delta T}$ is the strain that is observed in equilibrium when raising the temperature by an amount ΔT. We define x_1, x_2, and x_3 to be coordinates along the a, b, and c axes of the orthorhombic crystal, and u_1, u_2, and u_3 to be the components of the displacement. In our experiment the b axis is the surface normal, so that we also have the free surface boundary condition $\sigma_{2j} = 0$ at $x_2 = 0$. The equation of motion for the components of the displacement u_i is

$$\rho \frac{\partial^2 u_i}{\partial t^2} = \sum_j \frac{\partial \sigma_{ji}}{\partial x_j}. \qquad (4)$$

In this experiment the probe spot size is significantly smaller than that of the pump, and so we can set all spatial derivatives with respect to the lateral coordinates x_1 or x_3 to zero as long as we consider pump-probe delay times small compared to $D_{\text{laser}}/v_3 = 74$ ns, where $D_{\text{laser}} = 500$ μm is the smallest pump spot dimension and $v_3 = 6780$ m/s is the highest in-plane longitudinal acoustic wave speed [15]. The symmetry of the point group for TbMnO3 includes a twofold rotation about the b axis, and so we can also conclude that thermal stress at the surface cannot lead to nonzero displacements along in-plane directions, and so $u_1 = u_3 = 0$ everywhere. Thus, the only nonzero element of the strain tensor is $\eta_{22} = \partial u_2/\partial x_2$. The full solution for η_{22} is obtained by solving Eq. (4) in a manner analogous to that discussed by Thomsen *et al.* [16] for an isotropic system. The solution consists of a superposition of a strain wave that travels from the surface at

the longitudinal acoustic velocity v_2 and a time-independent strain profile that satisfies the condition $\sigma_{22} = 0$. In TbMnO$_3$ the room-temperature value of v_2 has been measured using Brillouin scattering [15] as 5468 m/s, and may increase somewhat at lower temperatures [17]. In the limit of instantaneous heating, the traveling wave contributes most significantly to the strain for times less than or comparable to $L_{\text{x-ray}}/v_2 = 14$ ps, where $L_{\text{x-ray}} = 76$ nm is the x-ray probe depth. Afterwards, we are left with the time-independent component which, using Eq. (3), can be written

$$\eta'_{22} = \frac{1}{C_{2222}} \sum_i C_{22ii} \eta_{ii}^{\Delta T} \tag{5}$$

thereby relating the transient strain to the temperature increase ΔT.

As shown in Fig. 2, our data show a laser-driven shift in the value of ϕ_B over a time scale of 20–40 ps (Table I). This is comparable to the timescale of 14 ps predicted for the traveling wave contribution to η_{22}, although somewhat longer. The longer timescale may indicate that the thermal stress does not appear instantaneously, but develops over several picoseconds and thereby extends the duration of the traveling wave component. Under the assumption that the observed dynamics in $\Delta\phi_B$ are indeed due to the thermal expansion scenario outlined above, we can estimate experimental values of $\eta_{22}(t)$ from the measurements of $\Delta\phi_B$ for the (0 2 4) and (1 3 −5) diffraction peaks. The Laue condition for scattering from a plane $(h\,k\,l)$ for a crystal under uniform normal b-axis strain η_{22} can be written as

$$2\mathbf{k}_i \cdot \mathbf{G} + \mathbf{G} \cdot \mathbf{G} = 0, \tag{6}$$

where

$$\mathbf{k}_i = \frac{2\pi}{\lambda}(\sin\phi_B\cos\alpha\,\hat{x}_1 - \sin\alpha\,\hat{x}_2 - \cos\phi_B\cos\alpha\,\hat{x}_3) \tag{7}$$

is the incoming x-ray wave vector and

$$\mathbf{G} = 2\pi\left(\frac{h}{a}\hat{x}_1 + \frac{k}{b(1 + \eta_{22})}\hat{x}_2 + \frac{l}{c}\hat{x}_3\right) \tag{8}$$

is the reciprocal lattice vector for the strained crystal. Here, $\lambda = 1.76$ Å is the x-ray wavelength, $\alpha = 0.5°$ is the incidence angle, and $a = 5.3167$ Å, $b = 5.8198$ Å, and $c = 7.3968$ Å are the unstrained lattice constants [18] at the initial temperature of 20 K. Equations (6)–(8) define an implicit relationship between ϕ_B and η_{22}, which can be differentiated to obtain

$$\left.\frac{d\eta_{22}}{d\phi_B}\right|_{\eta_{22}=0} = \frac{b^2}{k^2\lambda}\left(\frac{h}{a}\cos\phi_B + \frac{l}{c}\sin\phi_B\right), \tag{9}$$

where we used $\alpha \ll \lambda/b$ to simplify the relation. This allows us to relate our experimentally measured $\Delta\phi_B$ with a value of η_{22}. Figure 3(a) shows the result of converting the data of Fig. 2 to $\eta_{22}(t)$. We see that, as expected, the experimentally estimated strain dynamics do not depend on the lattice plane, but do depend on the pump fluence. At a fluence of 4.5 mJ/cm^2 the strain increases over a 20–40 ps timescale to approximately 0.008%, and for 9.0 mJ/cm^2 it increases to approximately 0.022%.

We can compare these experimentally measured values with the predictions of Eq. (5) under the assumption that all of
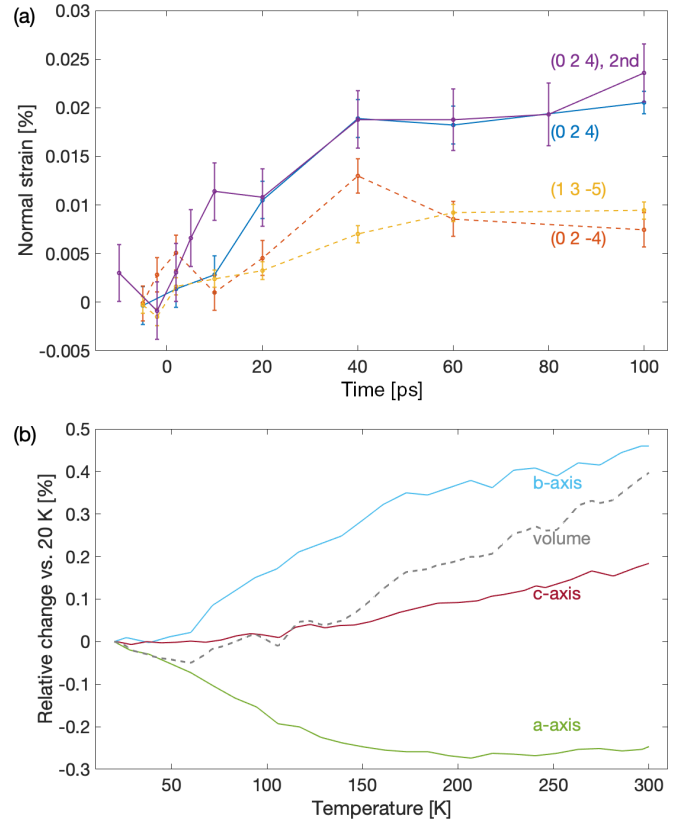

FIG. 3. (a) Photoinduced strain $\eta_{22}(t)$ along the b axis normal to the sample, estimated from Fig. 2 as described in the text. Full and dashed lines correspond to an absorbed fluence of 9.0 and 4.5 mJ/cm^2, respectively. (b) Axial strains and volume change as a function of temperature for bulk TbMnO$_3$ (from Blasco *et al.* [18]), relative to $T = 20$ K.

the absorbed energy from the pump pulse is used to increase the temperature of the sample along the excitation profile. As discussed in the Appendix, we estimate (assuming an initial temperature of 20 K) a temperature increase $\Delta T = 157$ K for the data collected on the (0 2 4) peak with 9.0 mJ/cm^2 absorbed fluence, and $\Delta T = 107$ and 93 K for the (0 2 −4) and (1 3 −5) peaks, respectively, at an absorbed fluence of 4.5 mJ/cm^2. To estimate the resulting strain, we need the equilibrium thermal strain tensor elements $\eta_{ii}^{\Delta T}$. These tensor elements are equivalent to the relative change in the lattice constants upon increasing temperature by ΔT. Figure 3(b) shows the relative change of the lattice constants under equilibrium conditions as a function of temperature measured by Blasco *et al.* [18]. Using these data to estimate $\eta_{22}^{\Delta T}$, in combination with experimental and DFT-based estimates of the elastic constants $C_{2211} = 114$ GPa, $C_{2222} = 212$ GPa, and $C_{2233} = 157$ GPa reported by Hemme *et al.* [15], we estimate a transient strain $\eta'_{22} = 0.266\%$ for an absorbed fluence of 9.0 mJ/cm^2, and strains $\eta'_{22} = 0.136\%$ and $\eta'_{22} = 0.113\%$ for the (0 2 −4) and (1 3 −5) peaks at an absorbed fluence of 4.5 mJ/cm^2, respectively. These estimates assume an initial temperature of 20 K; in the experiment there is likely some amount of average heating of the sample that raises the initial temperature to a somewhat higher value. As discussed in detail in the Appendix, increasing the assumed initial temper-

ature up to 65 K does not result in substantial changes to the estimated values of η'_{22}.

Notably, there is an order-of-magnitude difference between the estimated η'_{22} and the measured η_{22} at 100-ps pump-probe delay time. The measured strain $\eta_{22}(100 \text{ ps}) = 0.022\%$ can instead be directly used to calculate a temperature increase ΔT using Eq. (5). We estimate $\Delta T < 50$ K, which would correspond to an absorbed fluence approximately eight times lower than experimentally measured for the data on the (0 2 4) peak. These observations are consistent with those from magnetic order dynamics, mentioned above, where a 33-K spin temperature increase was determined following photoexcitation with a 9.0-mJ/cm^2 absorbed fluence [4].

V. DISCUSSION

To better understand the discrepancy between the measured and expected values of the strain, we have considered several possibilities. Potential technical issues include an incorrect estimate of the absorbed fluence and of the deposited energy density. Regarding the accuracy of our determination of the absorbed fluence, in addition to the TbMnO$_3$ samples we measured the structural response of bulk [411]-cut bismuth samples and found the data to be comparable to those from published reports [14], and certainly not inaccurate by a factor of 8. Calculating the energy density from the absorbed fluence requires knowing the penetration depth. As detailed above, we performed a careful estimate based on the optical conductivity data from Baldini *et al.* [7], taking into account the anisotropy in the material. Using other available optical conductivity data [8], obtained on samples with cuts different from ours, only leads to an enhancement of the discrepancy we observe. We can therefore rule out that the low transient strain values are due to inaccuracies in the determination of the experimental parameters.

We now consider possible explanations for the low values measured for $\eta_{22}(t)$ arising from the physical properties of the material. Summarizing the discussions above, 1.55 eV photons promote intersite d-d transitions between Mn^{3+} ions [8,9]. This electronic energy is then transferred to the lattice in the form of heat, typically in about a picosecond [7,19]. Heating the lattice creates expansive thermal stress near the surface, leading to expansive uniaxial strain due to coherent longitudinal acoustic phonons [16]. Given that the transient strain we measure is one order of magnitude smaller than that expected from the absorbed energy, there must be a bottleneck in one of these steps. Starting with the last step, it is difficult to imagine a process by which the lattice temperature would increase but the generated strain would be much smaller than expected. One possibility would be that heat conductivity is very high, such that the lattice cools down before strain has time to arise, but this is not expected in insulating TbMnO$_3$ [20]. The most likely scenario is that there is a bottleneck in the transfer of energy between the electronic and lattice subsystems. In addition to accounting for the discrepancy between expected and measured values of η_{22}, this scenario could lead to a delayed transfer of energy to the lattice, which would explain our observation that the strain develops on a somewhat longer timescale (Table I) than the 14 ps predicted by the sound velocity and the probe depth. Within this sce-

nario, one hypothesis would be that there is extremely weak coupling between the electron and lattice subsystems, i.e., an extremely low electron-phonon coupling constant (generally challenging to determine experimentally), which would extend the typical 1-ps timescale to beyond our 100-ps measurement window. This would be quite unexpected, and would hinder the production of strain waves, which relies on heating-induced stress being created at the surface of the sample on a timescale faster than that of acoustic wave propagation [16]. The small strain we measure could, however, still arise from direct coupling of excited electronic states to long-wavelength acoustic modes via deformation of the ionic potential, without any contribution from lattice heating. Theoretical modeling would be required to validate this hypothesis. An alternative hypothesis is that a large fraction of the electronic excitations gets trapped and does not immediately contribute to lattice heating. With such reduced lattice heating, the strain wave amplitude [16] would also decrease, consistent with the small value of $\eta_{22}(t)$ that we measure. One possible trapping mechanism that was proposed relies on the formation of anti–Jahn-Teller polarons [4,7,10,21]. According to this mechanism, the photoexcited Mn^{2+}-Mn^{4+} pair leads to a local relaxation of the Jahn-Teller distortion which prevents further hopping. The lifetime for this charge localization could well exceed the 100-ps pump-probe delay time accessible through our measurements. A direct test of this second hypothesis would be to use a technique sensitive to polaron formation, such as x-ray diffuse scattering or pair distribution function (for smaller polaron sizes). Independently of the origin of the bottleneck in the transfer of energy between the electronic and lattice subsystems, this scenario could in principle be confirmed by measuring the structural response of TbMnO$_3$ well beyond 100 ps and seeing whether the lattice slowly expands over time, or by using a technique sensitive to the lattice temperature such as transient Raman scattering. A lattice heating process that is too gradual may, however, be compensated by heat diffusion and therefore be difficult to detect.

As a final discussion topic, we address the potential relationship between magnetic and structural dynamics. Specifically, we are interested in finding out whether coupling to the lattice could be responsible for the relatively long 20–40 ps demagnetization timescale [2,4–7]. The magnetic order in TbMnO$_3$ is dictated by the superexchange interaction J between Mn^{3+} ions, bridged by O^{2-} ions. J can be modified by changing (i) the valence of the Mn^{3+} ions or (ii) the relative position of the Mn^{3+} and O^{2-} ions [22]. A change in ionic position can be achieved directly via strain or indirectly via heating, which leads to disorder and eventually to a change in the average position of the ions. Regarding (i), photoexcitation at 1.55 eV creates an Mn^{2+}-Mn^{4+} pair from two Mn^{3+} ions, meaning that it locally alters the valence of the Mn^{3+} ions. This process occurs in <1 ps [2,7,23] but is seen to not lead to a large enough disorder in the spin system for the long-range magnetic order to be affected on this short timescale [4,6], contrary to what is observed in, e.g., antiferromagnetic CuO [24] and ferrimagnetic compounds [25]. Trapped anti–Jahn-Teller polarons have been suggested as an explanation for the 20–40 ps demagnetization time [4,7,10,21], the picture being that hopping is restricted until the lattice expands due to heating. We have observed, however, that the lattice heats

up much less than expected up to 100 ps ($\Delta T < 50$ K instead of the expected $\Delta T = 157$ K), where the dynamics appear to saturate, a result that is consistent with demagnetization dynamics data from Johnson *et al.* [4] ($\Delta T = 33$ K), as discussed above. If anti–Jahn-Teller polarons do form, we therefore expect them to be more long lived than the 20–40 ps demagnetization timescale.

An alternative explanation for the demagnetization is related to (ii), where a change in ionic position causes a change in J by changing the hybridization between Mn^{3+} and O^{2-} ions [22,25–28]. Our measurements provide a direct estimate of $\eta_{22}(t)$ and can be summarized as follows. First, the value of $\eta_{22}(t)$ created by photoexcitation [Fig. 3(a)] is smaller than expected but nevertheless similar to the *b*-axis strain which accompanies a loss of magnetic order in the system [i.e., corresponding to a lattice temperature larger than T_{N_1}, Fig. 3(b)]. Second, strain propagates in TbMnO$_3$ on the same 20–40 ps timescale (Table I) as is observed for demagnetization. Third, the lattice heating which creates $\eta_{22}(t)$ (if any) necessarily occurs on a timescale faster than that of $\eta_{22}(t)$, although we could not measure the heating timescale directly. Based on these observations, we cannot unequivocally distinguish between direct strain and heating-induced disorder as the driving force behind the changes in the average ionic position which are responsible for demagnetization. However, independently of the details of the process, the fact that the demagnetization timescale coincides with the lattice dynamics and is over an order of magnitude slower than the electronic excitation enables us to conclude that the magnetic order in TbMnO$_3$ is robust to changes in the valence of the Mn^{3+} ions and controlled by changes in the position of the Mn^{3+} or O^{2-} ions.

VI. CONCLUSION

We have investigated the structural dynamics in the multiferroic phase of TbMnO$_3$ and have observed the appearance of tensile strain along the *b* axis, perpendicular to the sample surface, following photoexcitation at 1.55 eV. The 0.008% and 0.022% tensile strain at 100 ps is an order of magnitude smaller than the 0.113%–0.136% and 0.266% strain that arises in the system upon heating from 20 K up to the expected final temperature after photoexcitation with an absorbed fluence of 4.5 and 9.0 mJ/cm^2, respectively. We attribute this discrepancy to a bottleneck in the energy transfer between the electronic and lattice subsystems, possibly related to an extremely low electron-phonon coupling constant or to the formation of anti–Jahn-Teller polarons. Furthermore, the strain arises on the same 20–40 ps timescale that was reported for demagnetization, suggesting that the stability of the superexchange interaction that governs magnetic order in TbMnO$_3$, which remains robust against local variations in Mn^{3+} ionic valence, is controlled by the lattice structure. Our conclusions contribute to building a general phase diagram of rare-earth manganites, which is essential for our physical understanding of these systems as a whole, as well as for future plans to include them in technological devices.

Data underlying the results presented in this paper are available in the ETH Research Collection [29].

APPENDIX

For our estimates of the temperature-driven transient strain, the laser induced ΔT is estimated from the specific heat [30] and the energy density deposited by the pump pulse, which in turn depends on the absorbed fluence and the penetration depth. Given the strong in-plane anisotropy [7,8] of the [010]-cut TbMnO$_3$ samples, we estimate a penetration depth of 323 nm for a polarization along the crystallographic *a* axis and 671 nm for a polarization along the crystallographic *c* axis [7]. The projection of the *p*-polarized 1.55-eV pump wave vector onto the sample surface forms 49° and 29° angles with respect to the crystallographic *c* axis for the (0 2 4) and (1 3 −5) Bragg reflections, respectively, so that the deposited energy density depends on whether we are investigating the (0 2 4) or (1 3 −5) reflection. These projections are used to determine the ratio of the absorbed fluence along the *a* and *c* axes; the change in reflection is negligible. The deposited energy density along each axis is then calculated as the ratio between absorbed fluence and penetration depth, and the total deposited energy density as a weighted sum of those two contributions.

Another consideration is the temperature dependence of the specific heat, which makes the estimate of ΔT dependent on the initial temperature T_i. This is particularly relevant in the case where the sample temperature does not fully recover from the laser-induced heating before the arrival of the following pump pulse, an effect which we refer to as "average heating." We investigated possible effects from average heating by comparing the ϕ shift, $\Delta\phi_B$, between a ϕ scan on the (1 3 −5) Bragg reflection when the pump laser was off and one where it was on but arriving after the probe pulse and leading to an absorbed fluence of 4.5 mJ/cm^2. We observe a shift $\Delta\phi_B = 0.06°$, which can be related to the equilibrium temperature using Eqs. (6)–(8), setting $\eta_{22} = 0$, and the data of Fig. 3(b), namely the temperature-dependent values of lattice parameters *a*, *b*, and *c* in equilibrium. Based on this we estimate an effective initial temperature of 65 K. While this

observation changes the absolute temperature values in our discussion, the discrepancy we report between the measured $\eta_{22}(100\ \text{ps})$ and the expected η'_{22} [from Eq. (5)] remains, as does the fact that a much lower absorbed fluence would be required to explain our data. In detail, in the main text we assume $T_i = 20$ K and an absorbed fluence of 4.5 mJ/cm^2, from which we calculate $\Delta T = 93$ K for the $(1\ 3\ {-}5)$ Bragg reflection, and for which we would expect a strain $\eta'_{22} = 0.113\%$

[from Eq. (5)] instead of the $\eta_{22}(100\ \text{ps}) = 0.008\%$ that we measured. If we account for average heating by changing the initial temperature to $T_i = 65$ K and we keep the absorbed fluence of 4.5 mJ/cm^2, we obtain $\Delta T = 61$ K for the $(1\ 3\ {-}5)$ Bragg reflection. This leads to approximately the same expected strain $\eta'_{22} = 0.133\%$ as with $T_i = 20$ K, meaning that the predicted η'_{22} remains one order of magnitude larger than the measured $\eta_{22}(100\ \text{ps}) = 0.008\%$.

---

[1] T. Kimura, T. Goto, H. Shintani, K. Ishizaka, T. Arima, and Y. Tokura, Nature (London) **426**, 55 (2003).

[2] I. P. Handayani, R. I. Tobey, J. Janusonis, D. A. Mazurenko, N. Mufti, A. A. Nugroho, M. O. Tjia, T. T. M. Palstra, and P. H. M. van Loosdrecht, J. Phys.: Condens. Matter **25**, 116007 (2013).

[3] T. Kubacka, J. A. Johnson, M. C. Hoffmann, C. Vicario, S. de Jong, P. Beaud, S. Grübel, S.-W. Huang, L. Huber, L. Patthey, Y.-D. Chuang, J. J. Turner, G. L. Dakovski, W.-S. Lee, M. P. Minitti, W. Schlotter, R. G. Moore, C. P. Hauri, S. M. Koohpayeh, V. Scagnoli *et al.*, Science **343**, 1333 (2014).

[4] J. A. Johnson, T. Kubacka, M. C. Hoffmann, C. Vicario, S. de Jong, P. Beaud, S. Grübel, S.-W. Huang, L. Huber, Y. W. Windsor, E. M. Bothschafter, L. Rettig, M. Ramakrishnan, A. Alberca, L. Patthey, Y.-D. Chuang, J. J. Turner, G. L. Dakovski, W.-S. Lee, M. P. Minitti *et al.*, Phys. Rev. B **92**, 184429 (2015).

[5] P. Bowlan, S. A. Trugman, X. Wang, Y. M. Dai, S. W. Cheong, E. D. Bauer, A. J. Taylor, D. A. Yarotski, and R. P. Prasankumar, Phys. Rev. B **94**, 184429 (2016).

[6] E. M. Bothschafter, E. Abreu, L. Rettig, T. Kubacka, S. Parchenko, M. Porer, C. Dornes, Y. W. Windsor, M. Ramakrishnan, A. Alberca, S. Manz, J. Saari, S. M. Koohpayeh, M. Fiebig, T. Forrest, P. Werner, S. S. Dhesi, S. L. Johnson, and U. Staub, Phys. Rev. B **96**, 184414 (2017).

[7] E. Baldini, T. Kubacka, B. P. P. Mallett, C. Ma, S. M. Koohpayeh, Y. Zhu, C. Bernhard, S. L. Johnson, and F. Carbone, Phys. Rev. B **97**, 125149 (2018).

[8] M. Bastjan, S. G. Singer, G. Neuber, S. Eller, N. Aliouane, D. N. Argyriou, S. L. Cooper, and M. Rübhausen, Phys. Rev. B **77**, 193105 (2008).

[9] A. S. Moskvin, A. A. Makhnev, L. V. Nomerovannaya, N. N. Loshkareva, and A. M. Balbashov, Phys. Rev. B **82**, 035106 (2010).

[10] D. Talbayev, J. Lee, S. A. Trugman, C. L. Zhang, S. W. Cheong, R. D. Averitt, A. J. Taylor, and R. P. Prasankumar, Phys. Rev. B **91**, 064420 (2015).

[11] P. Beaud, S. L. Johnson, A. Streun, R. Abela, D. Abramsohn, D. Grolimund, F. Krasniqi, T. Schmidt, V. Schlott, and G. Ingold, Phys. Rev. Lett. **99**, 174801 (2007).

[12] B. Henrich, A. Bergamaschi, C. Broennimann, R. Dinapoli, E. F. Eikenberry, I. Johnson, M. Kobas, P. Kraft, A. Mozzanica, and B. Schmitt, Nucl. Instrum. Methods Phys. Res., Sect. A **607**, 247 (2009).

[13] B. L. Henke, E. M. Gullikson, and J. C. Davis, At. Data Nucl. Data Tables **54**, 181 (1993).

[14] S. L. Johnson, P. Beaud, C. J. Milne, F. S. Krasniqi, E. S. Zijlstra, M. E. Garcia, M. Kaiser, D. Grolimund, R. Abela, and G. Ingold, Phys. Rev. Lett. **100**, 155501 (2008).

[15] P. Hemme, C.-H. Li, P. Djemia, P. Rovillain, S. Houver, Y. Gallais, A. Sacuto, H. Sakata, S. Nowak, B. Baptiste, E. Charron, B. Perrin, L. Belliard, and M. Cazayous, J. Phys.: Condens. Matter **33**, 495402 (2021).

[16] C. Thomsen, H. T. Grahn, H. J. Maris, and J. Tauc, Phys. Rev. B **34**, 4129 (1986).

[17] G. Lalitha and P. V. Reddy, J. Magn. Magn. Mater. **320**, 754 (2008).

[18] J. Blasco, C. Ritter, J. García, J. M. de Teresa, J. Pérez-Cacho, and M. R. Ibarra, Phys. Rev. B **62**, 5609 (2000).

[19] S. Wall, D. Prabhakaran, A. T. Boothroyd, and A. Cavalleri, Phys. Rev. Lett. **103**, 097402 (2009).

[20] K. Berggold, J. Baier, D. Meier, J. A. Mydosh, T. Lorenz, J. Hemberger, A. Balbashov, N. Aliouane, and D. N. Argyriou, Phys. Rev. B **76**, 094418 (2007).

[21] P. B. Allen and V. Perebeinos, Phys. Rev. Lett. **83**, 4828 (1999).

[22] N. S. Fedorova, Y. W. Windsor, C. Findler, M. Ramakrishnan, A. Bortis, L. Rettig, K. Shimamoto, E. M. Bothschafter, M. Porer, V. Esposito, Y. Hu, A. Alberca, T. Lippert, C. W. Schneider, U. Staub, and N. A. Spaldin, Phys. Rev. Mater. **2**, 104414 (2018).

[23] J. Qi, L. Yan, H. D. Zhou, J. X. Zhu, S. A. Trugman, A. J. Taylor, Q. X. Jia, and R. P. Prasankumar, Appl. Phys. Lett. **101**, 122904 (2012).

[24] S. L. Johnson, R. A. de Souza, U. Staub, P. Beaud, E. Möhr-Vorobeva, G. Ingold, A. Caviezel, V. Scagnoli, W. F. Schlotter, J. J. Turner, O. Krupin, W. S. Lee, Y. D. Chuang, L. Patthey, R. G. Moore, D. Lu, M. Yi, P. S. Kirchmann, M. Trigo, P. Denes *et al.*, Phys. Rev. Lett. **108**, 037203 (2012).

[25] T. Ogasawara, K. Ohgushi, Y. Tomioka, K. S. Takahashi, H. Okamoto, M. Kawasaki, and Y. Tokura, Phys. Rev. Lett. **94**, 087202 (2005).

[26] A. V. Kimel, R. V. Pisarev, J. Hohlfeld, and T. Rasing, Phys. Rev. Lett. **89**, 287401 (2002).

[27] N. Thielemann-Kühn, D. Schick, N. Pontius, C. Trabant, R. Mitzner, K. Holldack, H. Zabel, A. Föhlisch, and C. Schüßler-Langeheine, Phys. Rev. Lett. **119**, 197202 (2017).

[28] D. Afanasiev, J. R. Hortensius, B. A. Ivanov, A. Sasani, E. Bousquet, Y. M. Blanter, R. V. Mikhaylovskiy, A. V. Kimel, and A. D. Caviglia, Nat. Mater. **20**, 607 (2021).

[29] DOI: 10.3929/ethz-b-000587465.

[30] R. Choithrani, M. N. Rao, S. L. Chaplot, N. K. Gaur, and R. K. Singh, J. Magn. Magn. Mater. **323**, 1627 (2011).